

Photonic Delay Processing with Centralized Etalon Cascade for Radio Beamsteering in Simplified 2×5 Phased-Array Radio Heads

Aina Val Martí, *Student Member, IEEE*, David Löschenbrand, *Member, IEEE*, Markus Hofer, *Member, IEEE*, Thomas Zemen, *Senior Member, IEEE*, and Bernhard Schrenk, *Member, IEEE*

Abstract— The adoption of beam-centric radio communication schemes calls for efficient methods of beamforming with multi-element antennas. We present a delay generation method that employs a shared and centralized cascade of Gires-Tournois etalons for element-by-element radio frequency beamsteering at remote radio heads, thus adding no complexity at the antenna site. We experimentally demonstrate beamsteering of up to 32° in combination with a 2×5 phased-array antenna operated at a radio carrier frequency of 3.5 GHz and transmitting 64-ary quadrature amplitude modulated, orthogonal frequency division modulated radio signals. The radio transmission performance over mobile optical fronthaul and free-space radio propagation is evaluated through offline error vector magnitude estimation and real-time transmission of high-definition video traffic. We further show carrier phase switching at 2 kHz using direct emission frequency modulation of the involved optical light sources, proving the proposed concept to support the fast tracking of mobile users.

Index Terms—Optical communication terminals, 5G, Mobile fronthaul, RF Beamforming, Microwave photonics

I. INTRODUCTION

IT is well known that the number of users demanding wireless data is hugely increasing. One solution to face the increase in capacity and spectral efficiency needed, is beamforming in combination with multi-element antennas, which allow to improve the capacity and data rates of wireless systems through mitigating interference at the same time. Together with centralized baseband processing, multiple-input / multiple-output (MIMO) schemes and the support for higher carrier frequencies, it is touted as the key enablers for future beam-centric radio access networks [1]. The formation of radio beams in mm-wave massive MIMO configurations can be accomplished by tailoring the complex amplitude of the radio carrier frequency. One way to do so is the adoption of a

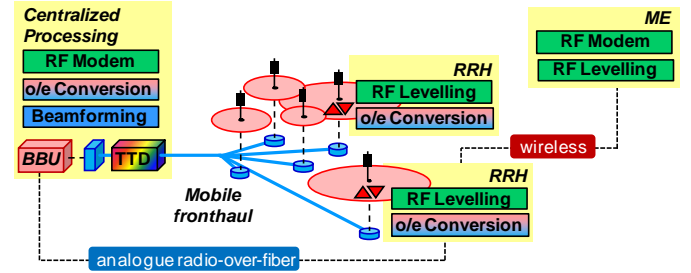


Fig. 1. Mobile optical fronthaul architecture that offloads beamforming to the centralized radio signal processing through integration of this function with opto-electronic (o/e) subsystems employed for analogue radio-over-fiber transmission between the BBU and the RRHs.

programmable true-time delay (TTD) associated to each antenna element [2]. While radio frequency (RF) based TTDs are difficult to implement over a wide frequency range, rendering them as a bandwidth-limiting factor, the off-loading of TTD to opto-electronic functions can mitigate this pivotal performance bottleneck: Transparent photonic beamforming methods have been shown to be compatible with wide signal bandwidths and a fast tuning response, which makes them of great interest.

The scientific contribution of this work is a method for photonic-assisted RF beamsteering with a centralized, shared delay generator. We accomplish this task without changing the outside fiber plant of the mobile fronthaul network, nor is beamforming circuitry employed at the distributed antenna sites. We will experimentally demonstrate beamsteering of up to 32° at 3.5 GHz with a phased-array 2×5 antenna configuration enabled through wavelength-specific delay tuning with a cascade of Gires-Tournois etalons, which is shared among wavelength sets. We experimentally confirm the quality of analogue radio-over-fiber and free-space RF signal transmission through offline error estimation and real-time data transfer. Furthermore, we demonstrate that the proposed concept can support for fast beamsteering at 2 kHz through direct frequency modulation of optical source lasers.

The paper is organized as follows. Section II relates the present work to the state-of-the-art in photonic beamforming demonstrations. Section III discusses and characterizes the beamforming method based on a shared etalon cascade. Section IV elaborates on the experimental setup used for performance evaluation. Section V elaborates on the beamsteering capability offered from the proposed concept,

Manuscript received February 28, 2022. This work was supported in part by the European Research Council (ERC) under the European Union's Horizon 2020 research and innovation programme (grant agreement No 804769). The work of D. Löschenbrand, M. Hofer and T. Zemen is funded within the Principal Scientist grant Dependable Wireless 6G Communication Systems (DEDICATE 6G) at the AIT Austrian Institute of Technology.

A. Val Martí, D. Löschenbrand, M. Hofer, T. Zemen and B. Schrenk are with the AIT Austrian Institute of Technology, Center for Digital Safety&Security, Giefinggasse 4, 1210 Vienna, Austria (phone: +43 50550-4131; fax: -4150; e-mail: bernhard.schrenk@ait.ac.at).

TABLE I
EXPERIMENTAL BEAMFORMING DEMONSTRATIONS WITH CONTINUOUS DELAY SETTING

Ref.	Year	Beam-forming	Principle for TTD / phase shifter	Compactness / Requirements	Optical loss	Demonstrated frequency band	Delay range	Steering angle	Tuning speed
[6]	2018	1×8	variable optical delay lines + multi-core fiber	fiber-optic delay line, requires multi-core feeder fiber	N/A	V band	±16.6 ps	30°	-
[7]	2018	1×2	variable optical delay lines + multi-core fiber	fiber-optic delay line, requires multi-core feeder fiber	3.5 dB	50 GHz	10 ps	180°	-
[8]	2021	1×3	WDM over single-mode fiber + coherent receiver	transistor-outline coherent receiver	35.6 dB	3.5 GHz	930 ns	20°	-
[9]	2015	4×4	programmable optical filter	bulk-optic device	N/A	25 GHz	1.4 ns	-	-
[10]	2005	1×4	photonic crystal fiber	specialized fiber-optics	3.4 dB	X band	±31 ps	23°	-
[11]	2017	1×8	dispersion compensating fiber array	fiber-optic transmission spans as delay generator	N/A	9.5 to 10.5 GHz	-	43°	12.5ns
[12]	2002	1×5	tunable linear chirped fiber grating	fiber-optic grating	N/A	20 GHz	25 ns	-	<100 μs
[13]	2020	1×4	chirped fiber Bragg grating array	fiber-optic grating	N/A	X + K _a bands	±250 ps	±36.8°	-
[14]	2016	1×4	chirped fiber Bragg grating in recirculating loop	fiber-optic grating, active recirculating loop	active loop	11.2 GHz	2.5 ns/trip	±60°	<1 ns
[15]	2021	3×3	raised cosine chirped fiber grating + Mach-Zehnder delay interferometer	fiber-optic grating	N/A	X band	61 ps/nm	(70°, 124°)	-
[16]	2016	8×8	variable optical delay lines + chirped fiber Bragg grating	fiber-optic grating and delay line	N/A	18 GHz	16 ps	(50°, 300°)	-
[17]	2021	1×8	chirped fiber grating + polarization-maintaining dispersion compensating fiber	fiber-optic grating	N/A	2.2 GHz	-100 ps/nm	18°	-
[19]	2014	1×10	tunable dual Fabry-Pérot etalon	multi-wavelength fiber ring laser with two Fabry-Pérot etalons	N/A	18 GHz	-	±42°	-
[20]	2022	2×5	Gires-Touanois etalon	bulk-optic device	5.3 dB	3.5 GHz	230 ps	32°	2 kHz

while Section VI evaluates the RF transmission performance. Section VII extends the evaluation through real-time signal analysis and video transmission. Section VIII investigates possibilities for fast switching of the carrier phase. Finally, Section IX, concludes the work.

II. RF BEAMFORMING ASSISTED BY PHOTONIC PHASE PROCESSORS

With the advent of cloud-based processing for radio access networks, the mobile optical fronthaul has become indispensable for a seamless connectivity between simplified remote radio heads (RRH) and centralized baseband units (BBU). Figure 1 presents such an optically hauled radio access network, which can feature either digitized or analogue radio-over-fiber transmission schemes [3]. For the simplified yet challenging method of analogue optical RF signal transmission, the optical layer can adopt additional functions aiming at all-optical signal processing. A representative scenario is the off-loading of carrier phase manipulation to optical TTD circuits in order to enable RF beamforming with multi-element antennas at the RRHs. In case that the optical TTD function can be facilitated in a shared manner, meaning that it is centralized at the central office (CO), the RRHs, which resemble the distributed tail-end units that feed the mobile equipment (ME) of the radio access network, can be further simplified (Fig. 1).

Towards the direction of TTDs, research work has pursued

optically-assisted RF beamsteering, with the aim to achieve a wide RF frequency range by virtue of the broadband nature of photonics, while minimizing the TTD loss at the same time. Waveguide-based or optically switched delay lines, such as shown in [4, 5], can be realized on a very small footprint exploiting photonic integrated circuits to create a TTD. Despite of the compactness and scalability, it can only provide a discrete setting for the introduced delay. With this, it does not address the continuous delay adjustment requirements of future radio networks, so that highly directional beam characteristics can be used with precise pointing. Towards this direction, Table I summarizes suitable technology concepts adopted in earlier beamforming demonstrations. A straightforward method is to set a variable optical delay per antenna element feed. In order not to increase the fronthaul fiber count when centralizing the required optical delay generator, multi-core fibers have been proposed to accomplish a per-core delay encoding when feeding the RRH [6, 7]. Continuous delay settings can also be obtained exploiting a shared dispersive media, such as the transmission fiber in [8, 9], specialized fiber [10, 11], or linearly chirped gratings [12-17]. In these schemes, a stable optical source is precisely tuned along a wavelength-dependent dispersion slope. As it is demonstrated in [15, 16], beamsteering can be accomplished in two dimensions, defining an elevation and azimuth angle for the radio beam at the same time. More compact elements that offer a tunable group delay have been demonstrated exploiting

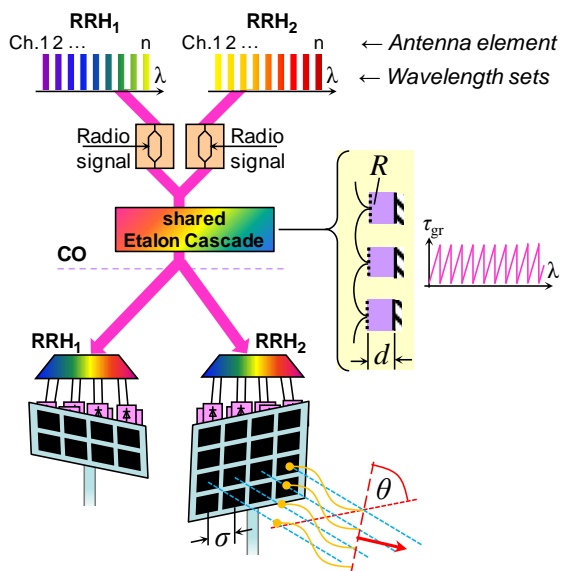


Fig. 2. Photonic RF beamsteering integrated with analogue radio-over-fiber transmission and accomplished through a centralized etalon cascade.

optical resonances. This method has been shown in combination with silicon micro-ring resonators [18] or silicon waveguide gratings [19]. However, the tuning mechanism can become complex and bandwidth limitations might arise. An option to reduce the complexity in tuning is provided through Gires-Tournois or Fabry-Pérot type etalons [20-23]. In this work, we extend our initial findings on shared delay dissemination through a Gires-Tournois etalon [23], by incorporating a second C-band wavelength set that is processed through the centralized etalon for the purpose of real-time radio signal transmission involving a high-definition video feed.

It shall be noted that the tuning speed of optically-assisted beamforming concepts can be fast, with response time in the μs to ns range, as evidenced in [11, 12, 14, 19]. Moreover, both low sub-6GHz and high RF carrier frequencies in the mm-wave range and beyond are supported [6, 7, 20].

III. SHARED ETALON CASCADE FOR RF BEAMFORMING

In order to accomplish beamsteering, the mobile optical fronthaul shall adopt the notion of analogue radio-over-fiber transmission in combination with optical signal processing. Figure 2 introduces the fundamental scheme of the beamsteering concept. The radio signal associated to a RRH is jointly modulated on an ensemble of optical carriers, herein referred to as wavelength set. This set is then demultiplexed at the antenna site to feed each antenna element with a different wavelength of this set. In order to introduce an element-specific phase shift for the RF carrier, the wavelength set is tailored in its spectral characteristics by traversing a TTD that ideally allows for a setting on a per-wavelength basis as the entire set passes through the shared delay element. The latter can be realized using an optical all-pass filter structure [24].

A. Gires-Tournois Etalon Cascade

This work employs a cascade of Gires-Tournois etalons [20, 21, 25, 26] for the purpose of optically-assisted RF

beamsteering. The etalons of the wavelength-shared cascade are characterized by an optical thickness d , a reflectance R at their front facet and a highly reflective back facet. The cascade of N etalons contributes with an all-pass behavior having a group delay spectrum given by the Gires-Tournois characteristics [27], according to

$$\tau_{gr}(\nu) = \sum_N \frac{2d}{c} \frac{1-R}{1+R-2\sqrt{R}\cos\left(\frac{4\pi\nu d}{c}\right)} \quad (1)$$

or

$$\tau_{gr}(\lambda) = \sum_N \frac{2d}{c} \frac{1-R}{1+R-2\sqrt{R}\cos\left(\frac{4\pi d}{\lambda}\right)} \quad (2)$$

where c is the speed of light. This function yields a linear periodic evolution over the optical frequency ν and approaches a sawtooth-like behavior with a large number N of etalons. Moreover, the period of the group delay function is adjusted to the dense wavelength division multiplexing (DWDM) spacing, meaning that the linear delay ramp repeats itself for each of the DWDM channels in a colorless manner.

The delay is set not through the etalon cascade, which remains passive, but through the injected optical frequencies. Since the optical source lasers can be precisely tuned with respect to their emission wavelength by either defining their temperature or current, this permits a continuous tuning of the group delay for each of the tributary channels that feed a single RRH. The robustness and accuracy of the spectral set-point is supported by the centralized approach for light generation, which permits the use of integrated DWDM sources [28] and joint temperature control for the entire comb, thus ruling out source-by-source variations.

The spectral tuning of the emission wavelength translates into an element-by-element setting of the RF carrier phase and, consequently, enabling RF beamsteering by an angle θ . In case of a linear phase evolution among the phase elements, which are spaced by the distance σ , this angle can be derived as

$$\theta = \arcsin\left(\frac{c \delta\tau}{\sigma}\right) \quad (3)$$

with $\delta\tau$ being the difference in group delay among two antenna elements.

The present work focuses on RF phase adjustment through the etalon cascade. Advanced beamforming schemes would require the adjustment of both, RF phase and amplitude, which could be simply accomplished by tuning the launch power of the DWDM comb wavelengths.

B. Characterization of the Etalon Cascade

Figure 3 reports the C-band group delay dispersion for the etalon cascade used in the later experiment. The group delay is further being related to the optical transmission of an athermal arrayed waveguide grating used as DWDM demultiplexer at

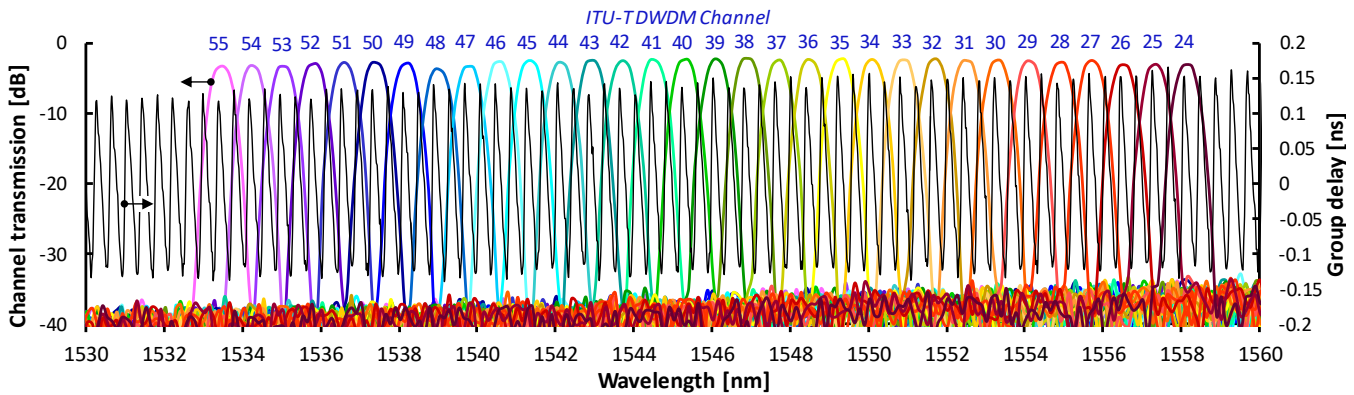


Fig. 3. Group delay dispersion of a centralized etalon cascade and associated demultiplexing function of an arrayed waveguide grating at the RRH.

the RRH to implement the signal feed for all of its antenna elements. The group delay dispersion features a periodicity of 50 GHz. It is further centered to the nominal channel wavelength of the ITU-T G.694.1 DWDM grid and allows delay tuning within the transmission window of the demultiplexer. As Fig. 4 shows, a range from -0.1 to 0.13 ns can be accommodated within the spectrally flat transmission window of a DWDM channel. As we will experimentally validate in Section V, this group delay dispersion makes the etalon cascade compatible with the RF phase-tuning requirements for phased-array antenna configurations for radio carrier frequencies in the sub-6GHz wireless band. Moreover, the wideband response of the etalon cascade and specifically its colorless nature enable its use as a centralized element. With this, it can be cost-shared among many antenna sites and further supports the notion for lean RRHs, for which RF and optical functions are ideally pooled at the CO that marks the head-end of the mobile fronthaul. On top of this, the loss associated to the beamformer element can be compensated through the booster amplifier employed to launch the feeder signal for the mobile optical fronthaul, which in case of a distributed integration at the RRH site could not be technologically justified.

Operation for higher RF carrier frequencies would require a re-design of the etalon cascade towards a wider periodicity. At the same time, the delay range should be reduced to relax the required accuracy for the spectral set-point that directly translates to the induced delay.

IV. EXPERIMENTAL SETUP

The experimental setup is presented in Fig. 5. It resembles a mobile fronthaul configuration with centralized beamsteering functionality integrated with the optical downlink transmitter, a RRH with a 2×5 configuration for its antenna elements, supplied through an analogue radio-over-fiber feed, and a short RF free-space propagation prior to the analysis of the received radio signal.

At the CO, a wavelength set $\lambda S1$ comprised of 10 DWDM channels ranging from $\lambda_1 = 1547.72$ to $\lambda_{10} = 1558.17$ nm is formed (Fig. 6). An orthogonal frequency division multiplexed (OFDM) radio signal with 128 sub-carriers featuring 64-ary quadrature amplitude modulation (QAM) is generated by an

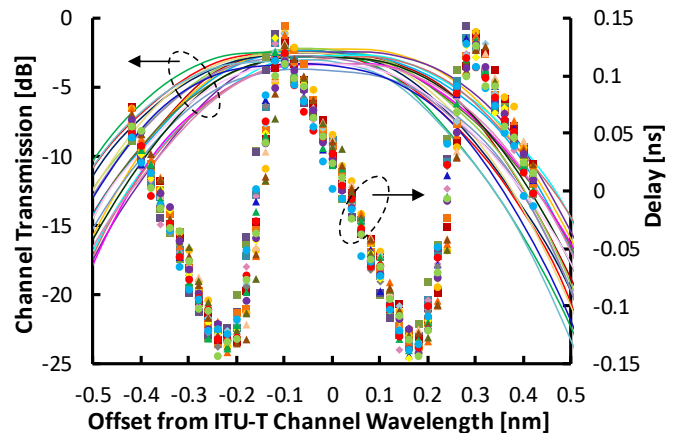


Fig. 4. Transmission of the DWDM demultiplexer and group delay over C-band channels relative to the center wavelength of the ITU-T DWDM grid.

arbitrary waveform generator (AWG). The OFDM signal has a bandwidth of 250-MHz and is centered at a radio carrier at $f_{RF} = 3.5$ GHz. The OFDM signal is modulated on all channels of the wavelength set by means of a Mach-Zehnder modulator (MZM) that is biased at its quadrature point. This first wavelength set will serve the evaluation of the radio signal transmission performance by means of off-line error vector magnitude (EVM) measurements.

Ten more DWDM channels within a second wavelength set $\lambda S2$ ranging from $\lambda_{11} = 1533.47$ to $\lambda_{20} = 1542.14$ nm (Fig. 6) are jointly modulated by another MZM, driven by a software-defined radio (SDR) unit. The SDR generates an OFDM signal at the same f_{RF} with a bandwidth of 20 MHz and 64-QAM sub-carrier modulation at a code rate of 3/4. The transmission performance for this second radio signal will be evaluated in terms of real-time block error ratio (BLER) and involves either pseudo-random data or traffic due to high-definition video-transmission.

Either comb of modulated DWDM channels is then spectrally processed by the cascade of Gires-Tournois etalons (GTEC), determining the delay setting for the constituent radio signals of all antenna elements. The GTEC has an optical transmission loss of 5.3 dB, which is compensated by an Erbium-doped fiber amplifier (EDFA) that is boosting the launched optical power to a level of 3 dBm/ λ with an average optical signal-to-noise ratio of 36.7 dB/0.1nm. It shall be

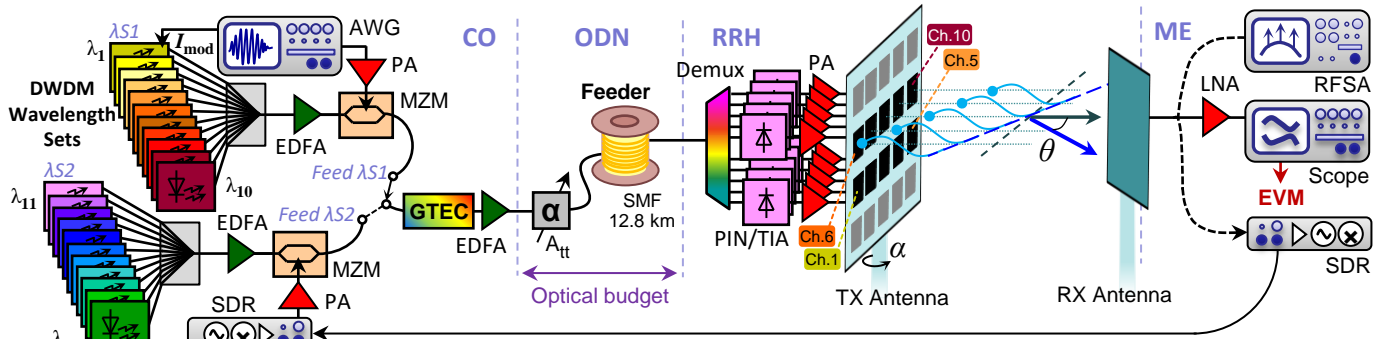


Fig. 5. Experimental setup of the mobile optical fronthaul with integrated RF beamsteering in downlink direction.

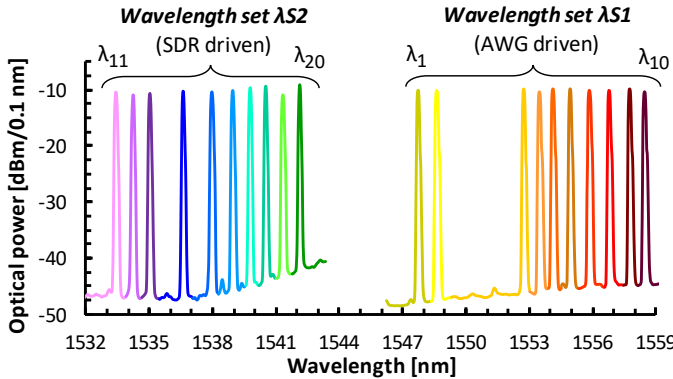


Fig. 6. Monitored wavelength sets carrying OFDM radio signals originating from AWG and SDR, respectively, and feeding the RRH alternately.

stressed that the wavelength sets are feeding a single RRH alternately, meaning that they are not simultaneously transmitted in this work.

The optical distribution network (ODN) employs a variable optical attenuator (A_{tt}) to simulate a passive trunk split and to set the optical budget of the ODN. The feeder span of the fronthaul is emulated by a 12.8-km long, ITU-T G.652B compatible single-mode fiber (SMF).

An arrayed waveguide grating at the RRH distributes the received DWDM channels of a wavelength set to its 2×5 antenna elements. The allocation of the comb was the following: the lower row was fed by the channels 1-5 of the AWG-driven wavelength set $\lambda S1$, while the upper row is supplied through channels 6-10. For the SDR-driven wavelength set $\lambda S2$, channels 11-15 and 16-20 apply. It shall also be noted that multiple RRHs can be in principle operated simultaneously on different wavelengths set. This can be for example accomplished through a DWDM demultiplexer with free spectral range property and waveband pre-filtering. After demultiplexing, the radio signals are converted to the RF domain through 10-GHz PIN receivers with transimpedance amplifier (TIA) backend. An additional RF amplifier serves as power amplifier for each of the antenna elements. It shall be stressed that care must be taken to avoid a path-length mismatch in the optical and RF domain once the wavelength set is demultiplexed. However, the maturity of photonic integrated circuit technology permits the integration of the entire opto-electronic RRH interface on a single chip, thus mitigating any mismatch due to inaccurate cable lengths.

The phased-array transmit antenna of the RRH is arranged

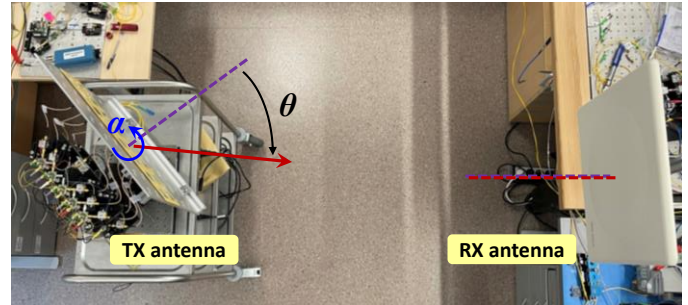


Fig. 7. Experimental arrangement for rotating phased-array transmit antenna and fixed, high-gain receive antenna.

on a rotation platform, which allows to set the pointing angle α of the antenna plane, as required for the evaluation of the beam steering efficiency. Contrarily, the receive antenna at the mobile equipment (ME) is fixed with respect to its orientation, pointing towards the transmit antenna (Fig. 7). The receive antenna had a directional gain of 23 dB, which greatly supports the suppression of RF reflections upon free-space radio signal transmission. An RF spectrum analyser (RFSAs) and a real-time oscilloscope were used to acquire the received RF power and the radio signal for the purpose of EVM estimation. Moreover, a second SDR unit has been used for real-time BLER measurement and video transmission. The uplink for the SDR units, which has not been in the scope of the present work, has been implemented through an electrical loop-back connection.

The RF phase adjustment per antenna element will practically require an auxiliary feedback channel to provide monitoring information on the actual RF phase setting, which can be easily acquired through a simple RF phase detector included with the RRH. This monitoring feature would further allow to mitigate the impact of dispersion at the feeder fiber, whose wavelength-dependent dispersion results in a small tilt in the RF phase setting among the antenna elements.

V. PHOTONIC RF BEAMSTEERING

The beamsteering functionality has been firstly evaluated by measuring the RF power for three different delay settings through the GTEC, which have been defined through the exact emission frequency set-point within the DWDM channel dedicated to the optical sources comprising the wavelength set. The chosen settings leading to a RF carrier phase shift of $\varphi = 0^\circ, 74^\circ$ and 150° (at $f_{RF} = 3.5$ GHz) between consecutive

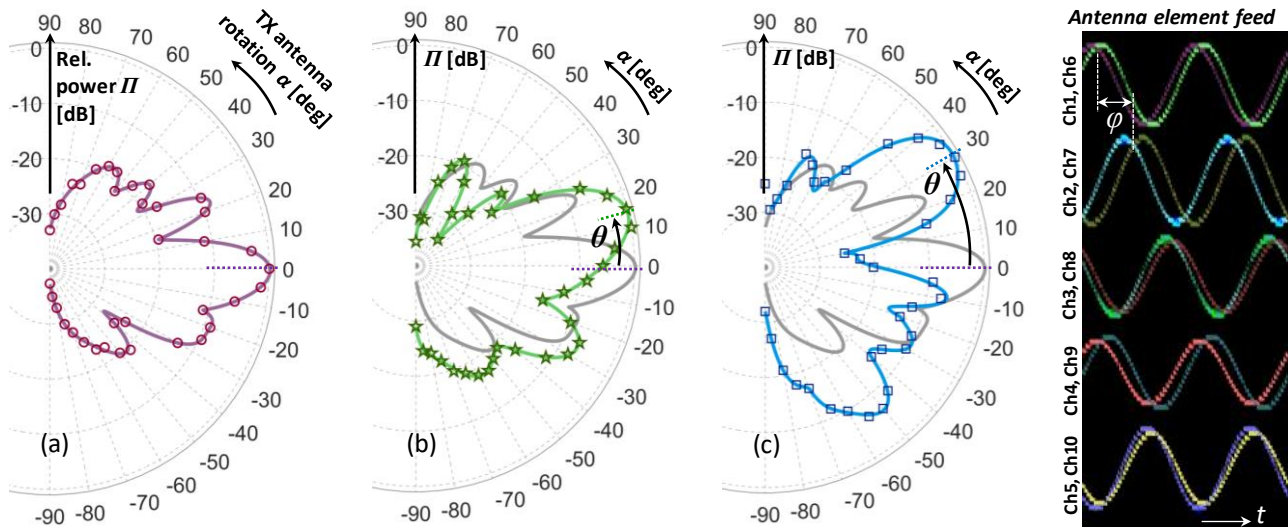


Fig. 8. Resulting beam profiles for (a) $\varphi = 0^\circ$, (b) $\varphi = 74^\circ$ and (c) $\varphi = 150^\circ$, with expected deflection angles $\theta_e = 0^\circ, 20^\circ$ and 44° , respectively. The exemplary RF carrier signals for the 2×5 phased-array antenna after photodetection of the wavelength set $\lambda S1$ at the RRH are shown for a configuration of $\varphi = 150^\circ$.

horizontal antenna elements, which have been monitored by tapping the RF outputs of the PIN/TIA receivers. Elements in the same column of the phased-array transmit antenna feature the same carrier phase. Consequently, the beam is deflected in azimuth θ . According to equation (2), the expected values for the aforementioned phase shifts are $\theta_e = 0^\circ, 20^\circ$ and 44° .

The acquired RF carrier at f_{RF} is shown in Fig. 8 after photodetection at the RRH. The traces are listed for all DWDM channels belonging to the wavelength set $\lambda S1$ and for the case that the RF carrier remains unmodulated at the CO. The phase shift of $\varphi = 150^\circ$, introduced by the delay setting of the GTEC, is clearly visible. As mentioned before, the elements in the same column of the antenna (Ch.1 and Ch.6, Ch.2 and Ch.7, and so on, see Fig. 3) had the same group delay and amplitude, and different phase shifts were assigned among the columns, depending on the desired beam steering angle.

In order to retrieve the beam profile, we rotated the transmit antenna by an angle α while acquiring the received RF power at the stationary receive antenna. Figure 7 relates the beam deflection angle θ and the rotation angle α to the experimental antenna setup.

Figure 8 presents the resulting beam profiles and the induced beamsteering effect for the three different beam deflection angles θ_e . For a phase shift of $\varphi = 0$, corresponding to an identical delay setting for all antenna elements, the main lobe points towards $\theta = -1^\circ$ (○) and has a full-width half maximum beam width of 12° . In this case, the power maximum is obtained when the antennas are facing each other. For the setting of $\varphi = 74^\circ$, the steering angle $\theta = 15^\circ$ (☆), meaning that the transmit antenna needs to be rotated by an angle $\alpha = \theta$ to obtain maximum power transmission to the receive antenna. A setting of $\varphi = 150^\circ$ yields $\theta = 32^\circ$ (□). We noticed an error $\theta - \theta_e$ between theory and experiment and a slight widening of the main lobe for an increased θ . Further investigations would require the use of an anechoic chamber in order to rule out RF fading effects due to reflections (see for example the asymmetry for $\varphi = 0$), leading to a more precise

acquisition of the beam profile. We did not observe a degrading effect due to transmission over the feeder fiber of the mobile fronthaul.

VI. ANALOGUE RADIO TRANSMISSION PERFORMANCE

After evaluating the principal beamsteering functionality we proceeded to evaluate the radio signal transmission performance for wavelength set $\lambda S1$. The corresponding results are reported in Fig. 9. We conducted two different measurements: First, we investigated the impact of optoelectronic signal conversion by acquiring the radio signals at one of the RRH elements after photodetection. Second, we acquired the radio signal after phased-array RF propagation.

Figure 9(a) shows the received RF spectra. Just after photodetection of the optically hauled radio signal, which is received at an optical power of -8 dBm, the OFDM spectrum has a flat envelope. This confirms that there is no bandwidth degradation introduced by the GTEC. The corresponding EVM, presented in Fig. 9(b), has an average EVM of 6.7% (●) at this optical feed level.

There were no RF interference fringes observed after RF phased-array propagation between transmit and receive antennas (Fig. 9(a)), owing to their good directional characteristics that suppress multi-path interference. Nevertheless, the roll-off in RF power towards higher frequencies is attributed to the fading inherent to RF propagation. We further noticed the effect of the phased-array gain through a slightly improved EVM of 5.9% (Fig. 9(b), ▲). The tilt in EVM performance towards higher values for a higher sub-carrier index is associated with the aforementioned fading.

The EVM dependence on the optical budget between CO and RRH is presented in Fig. 9(c). Results are again reported for the received radio signal at one antenna element. For the employed PIN/TIA receiver, the EVM antenna limit of 8% for 64-QAM transmission is reached at a received optical power of -9.8 dBm/λ. A better sensitivity could be accomplished through the use of avalanche photodetectors, which would

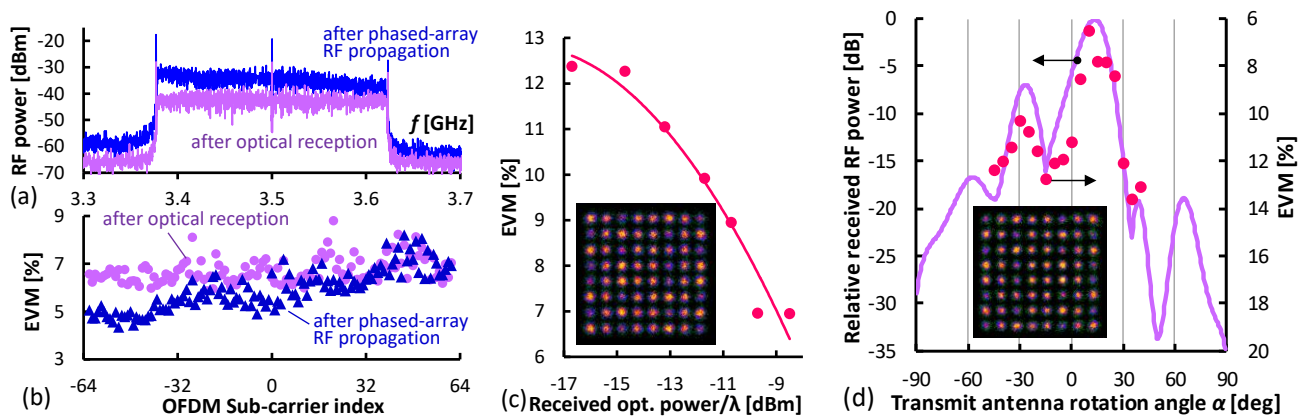


Fig. 9. (a) Received OFDM radio signal spectra before and after phased-array RF propagation and (b) corresponding EVM for an optical feed of -8 dBm. (c) EVM after photodetection, as function of the received optical power. (d) EVM and RF power after phased-array RF propagation for a setting of $\theta = 15^\circ$.

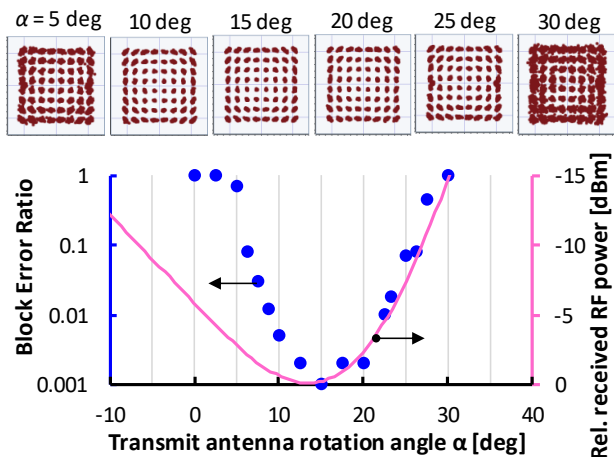


Fig. 10. BLER as function of the transmit antenna rotation. Results and constellations diagrams are shown for a beamsteering setting of $\theta = 15^\circ$.

further permit a higher dynamic range for simultaneous RF amplitude and phase adjustment in advanced beamforming schemes.

Figure 9(d) reports the EVM after RF propagation as function of the rotation angle α of the transmit antenna and relates it to the received RF power acquired earlier in Section V. Results are shown for the beamsteering setting yielding $\theta = 15^\circ$, corresponding to Fig. 8(b). The EVM (\bullet) evolves over α in a way that closely matches the received RF power and shows a minimum for $\alpha \approx \theta$. The clean 64-QAM constellation for the received 250-MHz wide OFDM radio signal evidences the good transmission performance over optical fronthaul and RF propagation paths.

VII. REAL-TIME SDR-BASED EVALUATION

Next, we have conducted real-time measurements of the BLER and conducted high-definition video streaming at 1920×1090 px² using the second RRH feed at the wavelength set λ_{S2} , which is driven by the SDR unit.

Figure 10 relates the measured BLER (\bullet) for a beamsteering setting of $\theta = 15^\circ$ to the corresponding received RF power of Fig. 8(b). Measurements are reported for an OFDM radio signal modulated by pseudo-random data as function of the rotation angle α for the transmit antenna. The

RF loss budget had been artificially increased in order to obtain error-free conditions only for the maximum received RF power at the center of the main lobe. In this way, the effect of an angular misalignment can be evaluated without being subject to BLER clipping effects. We found a good agreement for the rotation angles beyond $\alpha = \theta$ along the main lobe of the antenna beam, while the rapid decrease in BLER for decreasing α could not be elucidated. The constellations presented Fig. 10, obtained through real-time OFDM demodulation, show the increase in BLER associated with the power drop inherent to a walk-off from the main beam lobe.

Figure 11 presents long-term measurements of received RF power at the SDR unit of the ME, the associated BLER and the data throughput when streaming the video for more than one hour. The received power in Fig. 11(a) resembles a burst-like behavior, which resembles the idling periods of the SDR transmitter upon a partially loaded OFDM link. The corresponding data throughput with its burst-like behavior is included in Fig. 11(b). It features an average load of 5.8 Mb/s as required for video streaming. The resulting spread in received RF power is reported in Fig. 11(c) and indicates a stable received power for an active SDR transmitter. More importantly, the BLER, shown in Fig. 11(b), remains at an error-free level for the entire duration. We have not observed visual artifacts observed for the received video feed.

VIII. RF CARRIER PHASE SWITCHING

Mobility of users in beam-centric radio communication schemes or the provision of beams targeting multiple users might require a fast reconfiguration of the antenna beam. This necessity translates to a fast switching of the RF carrier phase.

To investigate this response of the proposed beamforming concept to this requirement, we introduced fast switching of the RF carrier phase through direct chirp modulation of the distributed feedback (DFB) laser associated to the DWDM feed channel at $\lambda_1 = 1547.72$ nm. The frequency modulation of the DFB emission, introduced through bias current modulation, amounts to 1 GHz/mA and is subsequently converted to a RF carrier phase change by the GTCE.

We synchronized the optically introduced RF carrier phase modulation with the generation of OFDM radio packets.

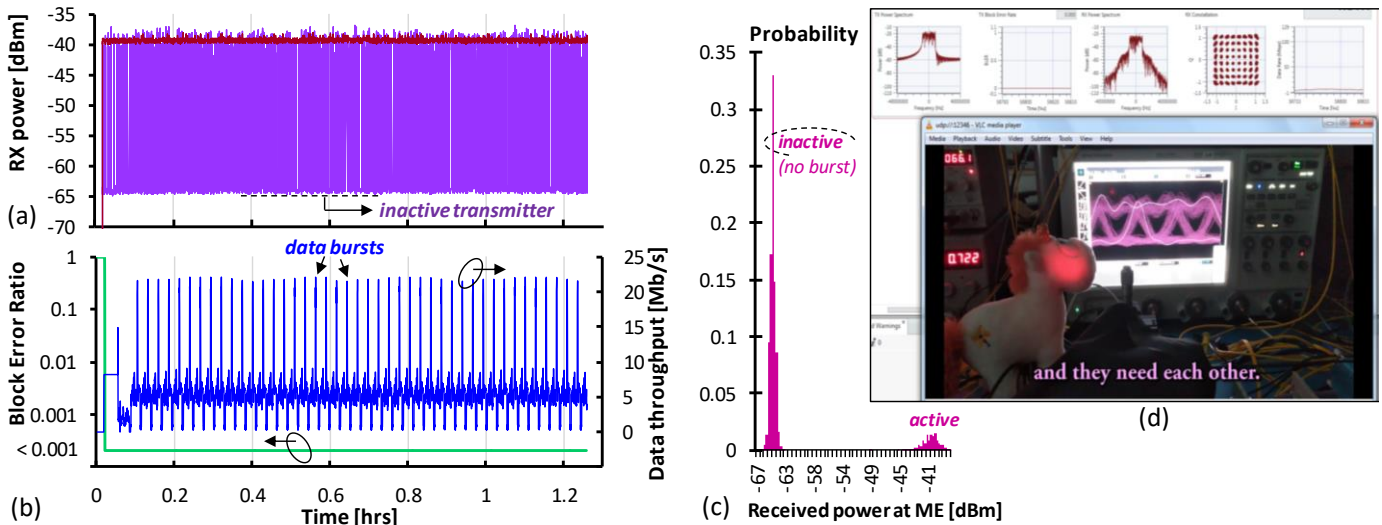


Fig. 11. (a) Received RF power at ME-based SDR unit. (b) BLER and data throughput. (c) Spread in received RF power. (d) Real-time video streaming.

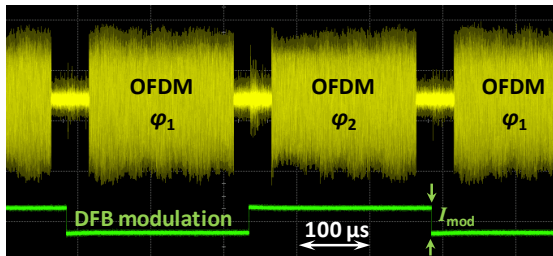


Fig. 12. RF carrier phase switching for consecutive OFDM packets, introduced through direct chirp modulation of the DFB source laser.

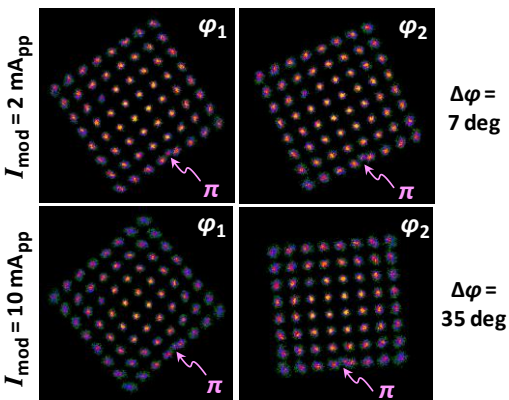


Fig. 13. RF carrier phase shifts for 64-QAM OFDM radio signal transmission at different DFB modulation settings.

Figure 12 shows the DFB drive and the skew-corrected received OFDM packets after photodetection at the RRH. The phase switching frequency was 2 kHz and a gap of 50 μ s has been inserted between two OFDM packets with relatively shifted RF carrier phase (φ_1 , φ_2) to account for phase transitions between the packets.

Figure 13 presents the constellations for both OFDM packets (φ_1 , $\varphi_2 = \varphi_1 + \Delta\varphi$) of a frame for the two peak-to-peak DFB modulation swings of $I_{\text{mod}} = 2 \text{ mA}_{\text{pp}}$ and $10 \text{ mA}_{\text{pp}}$. The received OFDM constellations are characterized by the position of the pilot tone π , which is used as an indicator for the introduced RF carrier phase shift. The relative alignment

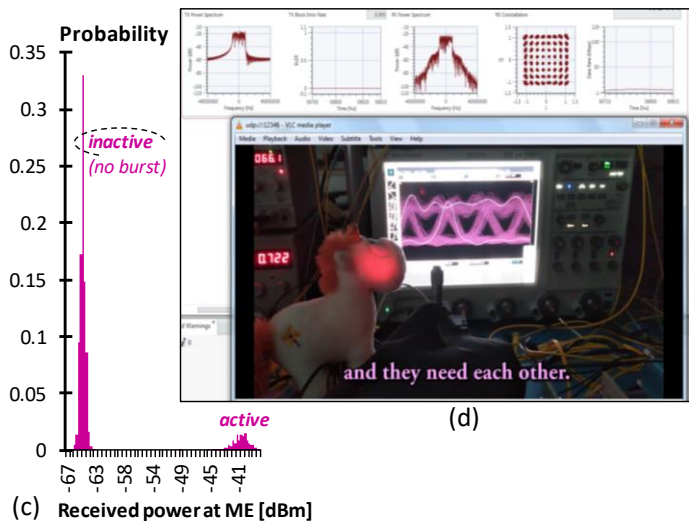


Fig. 14. EVM performance for the two OFDM packets with switched RF carrier phase.

between the RF carrier phases of the two OFDM packets is yielded with $\Delta\varphi = 7$ and 35° . This result further underpins the efficiency of the RF phase switching, which can be accomplished without extra components and at rather low drive levels.

In order to validate that the EVM performance is not impacted negatively, the EVM has been estimated for both OFDM packets. The corresponding EVM per subcarrier is presented in Fig. 14 for the first (\blacksquare) and second (\blacktriangle) OFDM packet. The difference in the average EVM between the two OFDM packets was 0.4%, which proves that the DFB current modulation for RF carrier phase switching does not introduce a penalty in the RF signal transmission.

Even though the switching of the RF carrier phase has not been applied to all antenna elements, it proves that the GTCE supports fast beamsteering in principle.

IX. CONCLUSION

An all-optical method for centralized RF beamsteering has been demonstrated in combination with a simplified RRH employing a 2×5 phased-array antenna configuration. The proposed concept builds on a GTEC with periodic group delay dispersion, making it compatible with DWDM overlay schemes and a per-element delay setting exploiting emission frequency tuning of the involved DWDM channels. For this purpose, the GTEC has been shown to adhere to the ITU-T DWDM grid and has enabled remote beamsteering of up to

32°. A good radio signal transmission performance has been validated through both, offline EVM measurements for a 250-MHz 64-QAM OFDM radio signal at 3.5 GHz. Measurements without and with beamsteering have proven that no penalty is introduced through the beamsteering concept, while the EVM performance agrees well with the expected beam profiles upon applied beam deflection. Real-time measurements supported by SDRs have confirmed the error-free operation through long-term measurements involving high-definition video transmission. Finally, we have evaluated fast RF carrier phase switching for one of the antenna elements through direct emission frequency modulation at 2 kHz, proving the concept to be compatible with deployment scenarios involving the tracking of mobile users at high velocity.

REFERENCES

- [1] S.A. Busar, K.M.S. Huq, S. Mumtaz, L. Dai and J. Rodriguez, "Millimeter-Wave Massive MIMO Communication for Future Wireless Systems: A Survey," *IEEE Comm. Surveys & Tutorials*, vol. 20, no. 2, pp. 836-869, Second Quarter 2018.
- [2] I. Ahmed *et al.*, "A Survey on Hybrid Beamforming Techniques in 5G: Architecture and System Model Perspectives," *IEEE Comm. Surveys & Tutorials*, vol. 20, no. 4, pp. 3060-3097, Fourth Quarter 2018
- [3] I. A. Alimi, A. L. Teixeira and P. P. Monteiro, "Toward an Efficient C-RAN Optical Fronthaul for the Future Networks: A Tutorial on Technologies, Requirements, Challenges, and Solutions", *IEEE Communications Surveys & Tutorials*, vol. 20, no. 1, pp. 708-769, Firstquarter 2018.
- [4] S. Fathpour, and N.A. Riza, "Silicon-photonics-based wideband radar beamforming: Basic design", *Optical Engineering*, vol. 49, no. 1, p. 018201, Jan. 2010.
- [5] B.L. Anderson *et al.*, "Hardware demonstration of extremely compact optical true time delay device for wideband electronically steered antennas," *IEEE/OSA J. Lightwave Technol.*, vol. 29, no. 9, pp. 1343–1353, May 2011.
- [6] T. Nagayama, S. Akiba, T. Tomura, and J. Hirokawa, "Photonics-Based Millimeter-Wave Band Remote Beamforming of Array-Antenna Integrated With Photodiode Using Variable Optical Delay Line and Attenuator," *IEEE/OSA J. Lightwave Technol.*, vol. 36, no. 19, pp. 4416-4422, Oct. 2018.
- [7] A. Morales, I. Tafur Monroy, F. Nordwall, and T. Sørensen. "50 GHz optical true time delay beamforming in hybrid optical/mm-wave access networks with multi-core optical fiber distribution," *Chinese Optics Letters*, vol. 16, no.4, p. 040603, 2018.
- [8] D. Milovančev, N. Vokić, D. Löschenbrand, T. Zemen and B. Schrenk, "Analogue Coherent-Optical Mobile Fronthaul with Integrated Photonic Beamforming", *IEEE J. Sel. Areas Comm.*, vol. 39, no. 9, pp. 2827-2837, 2021.
- [9] X. Ye, F. Zhang, and S. Pan, "Optical true time delay unit for multi-beamforming," *OSA Opt. Express*, vol. 23, no. 8, pp. 10002-10008, 2015.
- [10] Y. Jiang *et al.*, "Dispersion-enhanced photonic crystal fiber array for a true time-delay structured X-band phased array antenna," *IEEE Phot. Technol. Lett.*, vol. 17, no. 1, pp. 187-189, Jan. 2005.
- [11] L. Zhang *et al.*, "Photonic true time delay beamforming technique with ultra-fast beam scanning," *OSA Opt. Expr.*, vol. 25, no. 13, pp. 14524-14532, Jun. 2017.
- [12] Y. Liu, J. Yang, and J. Yao, "Continuous true-time-delay beamforming for phased array antenna using a tunable chirped fiber grating delay line," *IEEE Phot. Technol. Lett.*, vol. 14, no. 8, pp. 1172-1174, Aug. 2002.
- [13] N.K. Srivastava, R. Parihar, and S. K. Raghuvanshi, "Efficient Photonic Beamforming System Incorporating a Unique Featured Tunable Chirped Fiber Bragg Grating for Application Extended to the Ku-Band," *IEEE Trans. Microwave Theory and Tech.*, vol. 68, no. 5, pp. 1851-1857, Feb. 2020.
- [14] J. Zhang, and J. Yao, "Photonic true-time delay Beamforming using a switch-controlled wavelength-dependent recirculating loop," *IEEE/OSA J. Lightwave Technol.*, vol. 34, no. 16, pp. 3923-3929, Aug. 2016.
- [15] R. Kumar, and S. K. Raghuvanshi, "Efficient 2D Optical Beamforming Network With Sub Partitioning Capability Based on Raised Cosine Chirped Fiber Grating and Mach-Zehnder Delay Interferometer," *Phot. J.*, vol. 13, no. 3, p. 5500411, 2021.
- [16] B. Ortega, J. Mora, and R. Chulia, "Optical beamformer for 2D phased array antenna with subarray partitioning Capability," *Phot. J.*, vol. 8, no. 3, p. 6600509, Jun. 2016.
- [17] R. Kumar, S. K. Raghuvanshi, and D. Nadeem, "Chirped fiber grating and specialty fiber based multiwavelength optical beamforming network for 1x8 phased array antenna in S-band," *Elsevier Optik*, vol. 243, p. 167044, 2021.
- [18] Y. Liu *et al.*, "Ultra-Low-Loss Silicon Nitride Optical Beamforming Network for Wideband Wireless Applications," *IEEE/OSA J. Lightwave Technol.*, vol. 24, no. 4, p. 8300410, Jul. 2018.
- [19] G. Wang *et al.*, "Continuously tunable true-time delay lines based on a one-dimensional grating waveguide for beam steering in phased array antennas," *Appl. Opt.*, vol. 57, no. 18, pp. 4998-5003, Jun. 2018.
- [20] B.J. Vakoc, W.V. Sorin, and B.Y. Kim, "A Tunable Dispersion Compensator Comprised of Cascaded Single-Cavity Etalons," *IEEE Phot. Technol. Lett.*, vol. 17, no. 5, pp. 1043-1045, May 2005.
- [21] M. Sisto, M. Mousa Pasandi, L. Rusch, and S. LaRochelle, "Optical Phase and Amplitude Control for Beamforming with Cascades of Gires-Tournois Bragg Grating Filters," in *Proc. Opt. Fiber Comm. Conf. (OFC)*, San Diego, Unites States, Mar. 2010, paper OThF3.
- [22] H.B. Jeon, and H. Lee, "Photonic True-Time Delay for Phased-Array Antenna System using Dispersion Compensating Module and a Multiwavelength Fiber Laser," *J. Opt. Soc. Korea*, vol. 18, no.4, pp. 406-413, Sep. 2014.
- [23] A. Val Martí, D. Löschenbrand, T. Zemen, and B. Schrenk, "Radio Beamsteering for a 2x5 Remote Radio Head Assisted by a Shared Wideband Etalon Cascade", in *Proc. Opt. Fiber Comm. Conf. (OFC)*, San Diego, United States, Mar. 2022, paper W4C.4.
- [24] G. Lenz, B.J. Eggleton, C.R. Giles, C.K. Madsen, and R.E. Slusher, "Dispersive Properties of Optical Filters for WDM Systems," *IEEE J. Quantum Electron.*, vol. 34, no. 8, pp. 1390-1402, Aug. 1998.
- [25] M. Jablonski, Y. Takushima, and K. Kikuchi, "The Realization of All-Pass Filters for Third-Order Dispersion Compensation in Ultrafast Optical Fiber Transmission Systems," *IEEE/OSA J. Lightwave Technol.*, vol. 19, no. 8, pp. 1194-1205, Aug. 2001.
- [26] D.J. Moss *et al.*, "Tunable Dispersion and Dispersion Slope Compensators for 10 Gb/s Using All-Pass Multicavity Etalons," *IEEE Phot. Technol. Lett.*, vol. 15, no. 5, pp. 730-732, May 2003.
- [27] J.N. Damask, "Polarization Optics in Telecommunications", *Springer series in optical sciences*, New York, United States, 2004, ch. 4.3.2.
- [28] G.E. Hoefler *et al.*, "Foundry Development of System-On-Chip InP-Based Photonic Integrated Circuits," *IEEE J. Sel. Topics in Quantum Electron.*, vol. 25, no. 5, p. 6100317, Sep. 2019.